

Experimental Investigation of Geometric Quantum Speed Limits in an Open Quantum System

Diego Paiva Pires,¹ Eduardo R. deAzevedo,² Diogo O. Soares-Pinto,² Frederico Brito,^{3,2} and Jefferson G. Filgueiras^{4,2,5}

¹*Departamento de Física, Universidade Federal do Maranhão,*

Campus Universitário do Bacanga, 65080-805, São Luís, Maranhão, Brazil

²*Instituto de Física de São Carlos, Universidade de São Paulo, CP 369, 13560-970, São Carlos, São Paulo, Brazil*

³*Quantum Research Center, Technology Innovation Institute, P.O. Box 9639, Abu Dhabi, UAE*

⁴*Instituto de Química, Universidade Federal Fluminense,*

Outeiro de São João Batista, s/n, Niterói, 24020-141 RJ, Brazil

⁵*Instituto de Física, Universidade Federal do Rio de Janeiro, CP 68528, 21941-972, Rio de Janeiro, RJ, Brazil*

We studied geometric quantum speed limits (QSL) of a qubit subject to decoherence in an ensemble of chloroform molecules in a Nuclear Magnetic Resonance experiment. The QSL is a fundamental lower bound on the evolution time for quantum systems undergoing general physical processes. To do so, we controlled the system-reservoir interaction and the spin relaxation rates by adding a paramagnetic salt, which allowed us to observe both Markovian and non-Markovian open system dynamics for the qubit. We used two distinguishability measures of quantum states to assess the speed of the qubit evolution: the quantum Fisher information (QFI) and Wigner-Yanase skew information (WY). For non-Markovian dynamics and low salt concentrations, we observed crossovers between QSLs related to the QFI and WY metrics. The WY metric sets the tighter QSL for high concentrations and Markovian dynamics. We also show that QSLs are sensitive even to small fluctuations in spin magnetization.

One of the core concepts of quantum mechanics is the uncertainty principle. While this relationship is well known for non-commuting observables, e.g., position and momentum, the time-energy uncertainty relation has been controversial over decades, resulting in several attempts to address this issue [1, 2]. In their seminal work, Mandelstam and Tamm (MT) [3] reinterpreted this question by introducing the concept of quantum speed limit (QSL), which is a threshold imposed by quantum mechanics to the minimum evolution time between two orthogonal states. QSLs have been addressed for either closed and open quantum systems [4–16], and find applications ranging from quantum many-body systems [17–24], to quantum thermodynamics [25–28].

Information geometry is a powerful tool to study QSLs. In this setting, one finds a general framework providing an infinite family of QSLs based on contractive Riemannian metrics on the space of quantum states, which applies to any physical process [29]. In this scenario, the QSL relates to a certain information-theoretic distinguishability measure built for a set of quantum states, pure or mixed, separable or entangled, valid for closed and open systems. In addition, QSL bounds were investigated theoretically using matrix norms, e.g., Schatten p-norms, applied to the generator of the nonunitary dynamics [30].

Recent studies include an analysis of QSLs for driven quantum systems under Markovian evolution [31]. Importantly, such an approach allowed the investigation of the influence of non-Markovianity on the speed of evolution, finding that, for the Jaynes-Cummings model, its effect could lead to a faster evolution [32]. These results triggered studies of QSLs for particular choices of quantum channels focusing on how the degree of non-Markovianity could affect the tightness of QSL bounds [33–37]. Overall, non-Markovian dynamics present an intricate physical structure, allowing the revivals of genuine quantum resources during the evolution, for example, quantum coherence, thus contrasting with the typical monotonic loss observed in Markovian scenarios [38]. Noteworthy,

QSL depends on the initial state and the dynamical map governing the system evolution, showing the absence of a general connection between non-Markovianity and the speed of evolution of a quantum system [39–41].

Recently, an experimental measurement of the QSL time in a trapped single-atom system showed a crossover between the Mandelstam-Tamm and Margolus-Levitin bounds, with the latter dominating the dynamics for longer times [42]. We also mention the experimental discussion of the MT bound for time-dependent Hamiltonians with nuclear spin systems [43]. Despite all theoretical advances in understanding QSLs and experimental achievements for closed quantum systems, the field still lacks experimental studies exploring and certifying the machinery developed for open quantum systems. That happens due to the challenge of controlling the system-environment interaction and configuration, which determines the Markovian or non-Markovian character of the evolution.

In this work, we assess geometric QSLs in an open quantum system, by controlling just two parameters of the bath: the relaxation times of the hydrogen and carbon nuclear spins of an ensemble of chloroform molecules in a liquid-state Nuclear Magnetic Resonance (NMR) experiment. We control the relaxation rates of the carbon and hydrogen nuclear spins by adding a paramagnetic salt to the solution, allowing us to observe the transition from non-Markovian to Markovian regimes in the dynamics [44, 45]. Then, we investigate how the speed of evolution is affected under different experimental conditions. For non-Markovian dynamics and low salt concentrations, we observe crossovers between quantum speed limits defined by the quantum Fisher information and the Wigner-Yanase skew information metrics. The occurrence of these crossovers is related to the character of the systems time evolution. In high concentrations, the Wigner-Yanase metric sets the tighter quantum speed limit bound when the system undergoes non-Markovian or Markovian dynamics.

Model — In our experiments, we consider a two-qubit system encoded on the nuclear spins of the ^{13}C and ^1H of an

ensemble of chloroform (CHCl_3) molecules in liquid-state at room temperature. The interaction between the spins is given by the Hamiltonian $H = \frac{\pi J}{2} \sigma_z \otimes \sigma_z$, where J is the strength of the interaction, and σ_i is the i -th Pauli matrix ($i = x, y, z$). For simplicity, we set $\hbar = 1$. The two-qubit system initiates in a thermal equilibrium state $\rho_T^{CH} \approx [(1 - \epsilon_C)/4] \mathbb{I} \otimes \mathbb{I} + (\epsilon_C/2) |0\rangle\langle 0| \otimes \mathbb{I} + (\epsilon_H/4) \mathbb{I} \otimes \sigma_z$, which is valid at the high-temperature limit ($\epsilon_l \ll 1$), with $\epsilon_l = \hbar\omega_l/k_B T$ and $\omega_{C,H}$ is the ^{13}C (^1H) Larmor frequency, k_B is the Boltzmann constant, and T is the temperature. Since we are interested in the ^{13}C magnetization, one can discard the first and third terms in state ρ_T^{CH} , such that the density matrix for the ^{13}C spin is given, up to normalization, by $\rho^C = \text{Tr}_H(\rho_T^{CH}) \approx |0\rangle\langle 0|$ [44]. We obtain the initial state for our experiments after a $\pi/4$ rotation on the y -axis, resulting in $\rho_0^C = (1/2)(\mathbb{I} + (\sigma_x + \sigma_z)/\sqrt{2})$.

To model the open system dynamics of the carbon nuclear spin, we followed the description in Refs. [44, 46]. The proton spin becomes a source of the decoherence for the carbon spin when the condition $T_{1,H} \approx 1/J$ is satisfied. Under this condition, the flips on the proton spin due to $T_{1,H}$ occur at the same time scale as the evolution caused by the scalar coupling, introducing an effective time dependence on this coupling. This results in a faster decay of the system magnetization, known as scalar relaxation [47]. This process is inhomogeneous in time, with a correlation time given by the minimum between $T_{1,H}$ and $1/J$ [44, 46, 48]. By modulating $T_{1,H}$ through paramagnetic relaxation, we can control the degree of non-Markovianity of the ^{13}C open-system dynamics. In the limit of fast correlation time, $T_{1,H} \ll 1/J$, i.e., for high concentrations of the paramagnetic salt, we observe Markovian dynamics for the system dephasing.

We consider a phase-damping channel to model the spin-spin relaxation of the ^{13}C spin and a single bit-phase flip channel for both spin-lattice and spin-spin relaxations of the ^1H spin, since $T_{1,H} \approx T_{2,H}$ for all experimental configurations discussed throughout our results. The Kraus operators for the phase damping are $K_1 = \sqrt{q_t} \mathbb{I} \otimes \mathbb{I}$ and $K_2 = \sqrt{1 - q_t} \sigma_z \otimes \mathbb{I}$, with $q_t = (1 + e^{-t/2T_{2,C}})/2$. For the bit-phase flip, one gets $\mathcal{E}_1 = \sqrt{p_t} \mathbb{I} \otimes \mathbb{I}$ and $\mathcal{E}_2 = \sqrt{1 - p_t} \mathbb{I} \otimes \sigma_y$, where $p_t = (1 + e^{-t/2T_{1,H}})/2$. Here $T_{1,H}$ and $T_{2,C}$ define the characteristic time of the bit-phase flip channel and phase damping channel, respectively.

In this scenario, the state of the two-qubit system during the evolution is obtained by the application of the Kraus operators to the initial state, when partitioning the evolution time $0 \leq t \leq \tau$ into N equal steps of size $\Delta t = \tau/N$, with $J\Delta t \ll 1$. Hence, by iterating such a process, with $\Delta t \rightarrow 0$ ($N \rightarrow \infty$), and tracing out the hydrogen degrees of freedom, one obtains the single-qubit marginal state as follows

$$\rho_t^C = \frac{1}{2} (\mathbb{I} + \langle \sigma_x \rangle_t \sigma_x + \langle \sigma_z \rangle_0 \sigma_z), \quad (1)$$

where $\langle \sigma_x \rangle_t = \xi(t) \langle \sigma_x \rangle_0$ stands for the transversal magnetization of the ^{13}C (hereafter the system), with

$$\begin{aligned} \xi(t) = 2e^{-t/2T_{2,C}} e^{-t/4T_{1,H}} & \left[\frac{t}{4T_{1,H}} \text{sinc} \left(\frac{t}{4T_{1,H}} \sqrt{16\pi^2 J^2 T_{1,H}^2 - 1} \right) \right. \\ & \left. + \cos \left(\frac{t}{4T_{1,H}} \sqrt{16\pi^2 J^2 T_{1,H}^2 - 1} \right) \right], \end{aligned} \quad (2)$$

with $\text{sinc}(x) := \sin x/x$, and $\xi(0) = 1$. From now on, we will omit the superscript in Eq. (1) and define ρ_t as the single-qubit state of the ^{13}C nuclear spin.

The function $\xi(t)$ in Eq. (2) encodes the nonunitary signatures in the dynamics of the two-level system. Furthermore, it shows how reducing $T_{1,H}$ increases the role of the ^1H nuclear spin as the main source of decoherence, with the dynamics dominated by the $\text{sinc}(\bullet)$ term in Eq. (2) and the oscillations due to the scalar interaction disappearing for $T_{1,H} \ll 1/J$. Thus, to evaluate the geometric QSL of a given Riemannian metrics, we prepare the state ρ_0 by the application of a single $(\pi/4)$ pulse on the y -axis and let the system evolve according to Eq. (2). We control the relaxation rates $1/T_{1,H}$ and $1/T_{2,C}$ by adding the paramagnetic salt iron(III) acetylacetone (Fe(acac)₃) to the solution, with the relaxation rates growing linearly with the concentration of Fe(acac)₃ [47]. In the Supplementary Material [49] (see also Ref. [50] therein), we present technical details about the experiment and sample preparation.

Quantum speed limits for open system dynamics — The quantum speed limit (QSL) is related to the distinguishability of quantum states from a geometric perspective [29]. We remind that the so-called Morozova-Čencov-Petz (MCP) theorem states that the convex space of quantum states is endowed with a family of contractive Riemannian metrics [51, 52]. In this sense, the nonuniqueness of distinguishability measures of quantum states implies a class of geometric QSLs that can be exploited in the search for tighter bounds. Here, we discuss the QSL time for the single-qubit state ρ_t in Eq. (1). The evolution of this state draws a path γ in the space of quantum states connecting initial ρ_0 and final ρ_τ states. The MCP theorem states that the length $\ell_\gamma^f(\rho_0, \rho_\tau)$ of such path depends on some chosen contractive Riemannian metric related to a given Morozova-Čencov (MC) function f [51, 52]. Hereafter, we will restrict our analysis to two paradigmatic metrics: the quantum Fisher information (QFI) and the Wigner-Yanase skew information (WY). In particular, focusing on the single-qubit state in Eq. (1), the length of the path depicted by the nonunitary evolution of the state ρ_t becomes

$$\ell_\gamma^f(\rho_0, \rho_\tau) = \frac{1}{2} \int_0^\tau dt \sqrt{h_t^f} \left| \frac{d\langle \sigma_x \rangle_t}{dt} \right|, \quad (3)$$

with

$$h_t^{\text{QFI}} := \frac{1 - \langle \sigma_z \rangle_0^2}{1 - \langle \sigma_x \rangle_t^2 - \langle \sigma_z \rangle_0^2}, \quad (4)$$

and

$$\begin{aligned} h_t^{\text{WY}} := & \frac{\langle \sigma_x \rangle_t^2}{\left(\langle \sigma_x \rangle_t^2 + \langle \sigma_z \rangle_0^2 \right) \left(1 - \langle \sigma_x \rangle_t^2 - \langle \sigma_z \rangle_0^2 \right)} \\ & + \frac{2\langle \sigma_z \rangle_0^2 \left(1 - \sqrt{1 - \langle \sigma_x \rangle_t^2 - \langle \sigma_z \rangle_0^2} \right)}{\left(\langle \sigma_x \rangle_t^2 + \langle \sigma_z \rangle_0^2 \right)^2}. \end{aligned} \quad (5)$$

For details in the proof of Eqs. (3), (4), and (5), see the Supplemental Materials [49]. We point out that γ is an arbitrary

path connecting states ρ_0 and ρ_τ , and its length need not be the shortest one [53]. Indeed, for a given Riemannian metric on the space of quantum states, there exists a geodesic path with minimum length $\mathcal{L}^f(\rho_0, \rho_\tau)$ followed by the evolved state ρ_t when going from ρ_0 to ρ_τ . On the one hand, the geodesic length related to the QFI metric is given by the Bures angle, $\mathcal{L}^{\text{QFI}}(\rho_0, \rho_\tau) = \arccos[\sqrt{F(\rho_0, \rho_\tau)}]$, where the Uhlmann fidelity related to initial ρ_0 and final ρ_τ single-qubit states yields

$$F(\rho_0, \rho_\tau) = \frac{1}{2} \left[1 + \langle \sigma_x \rangle_0 \langle \sigma_x \rangle_\tau + \langle \sigma_z \rangle_0^2 + \prod_{s=0,\tau} \sqrt{1 - \langle \sigma_x \rangle_s^2 - \langle \sigma_z \rangle_0^2} \right]. \quad (6)$$

On the other hand, the WY metric implies the geodesic length known as Hellinger angle, $\mathcal{L}^{\text{WY}}(\rho_0, \rho_\tau) = \arccos[A(\rho_0, \rho_\tau)]$, while the quantum affinity for single-qubit states is given by

$$A(\rho_0, \rho_\tau) = \frac{\langle \sigma_x \rangle_0 \langle \sigma_x \rangle_\tau + \langle \sigma_z \rangle_0^2 + \prod_{s=0,\tau} \left(1 + \sqrt{1 - \langle \sigma_x \rangle_s^2 - \langle \sigma_z \rangle_0^2} \right)}{\prod_{s=0,\tau} \left(\sqrt{1 + \sqrt{\langle \sigma_x \rangle_s^2 + \langle \sigma_z \rangle_0^2}} + \sqrt{1 - \sqrt{\langle \sigma_x \rangle_s^2 + \langle \sigma_z \rangle_0^2}} \right)}. \quad (7)$$

The geodesic length constitutes a lower bound for the length of the path drawn by the above dynamical evolution, i.e., $\mathcal{L}^f(\rho_0, \rho_\tau) \leq \ell_\gamma^f(\rho_0, \rho_\tau)$. Solving this inequality as a function of time, one finds the QSL time related to the nonunitary evolution of the single-qubit state in Eq. (1). In this setting, any distinguishability measure of quantum states gives rise to a different geometric QSL. The contractive Riemannian metric whose geodesic length \mathcal{L}^f is effectively tailored to the nonunitary dynamical evolution depicted by the length ℓ_γ^f is the one that signals the tightest QSL [29]. To investigate the tightness of a given geometric QSL, we set the relative error

$$\delta_\gamma^f := \frac{\ell_\gamma^f(\rho_0, \rho_\tau) - \mathcal{L}^f(\rho_0, \rho_\tau)}{\mathcal{L}^f(\rho_0, \rho_\tau)}. \quad (8)$$

For a given metric, Eq. (8) indicates how far the dynamical evolution is from the respective geodesic path, and is expected to approach zero when both coincide such that the QSL bound saturates. Here, the tightest geometric QSL for the nonunitary dynamics of the single-qubit state is obtained after minimizing the quantity δ_γ^f over the two aforementioned information-theoretic quantifiers, namely, QFI and WY metrics. In addition, we consider the relative difference $\delta_\gamma^{\text{QFI}} - \delta_\gamma^{\text{WY}}$ as a criterion to testify the tightest QSL, i.e., for $\delta_\gamma^{\text{QFI}} - \delta_\gamma^{\text{WY}} > 0$ we have that WY metric assigns the tighter QSL, while for $\delta_\gamma^{\text{QFI}} - \delta_\gamma^{\text{WY}} < 0$ the QFI metric sets the tightest lower bound.

In the following, we discuss geometric QSLs for the single-qubit state by focusing on QFI and WY metrics. To do so, we compare numerical simulations of the open-system dynamics with the results calculated using experimental data. The quantum state undergoes a nonunitary evolution exhibiting both non-Markovian and Markovian regimes. In the limit of high

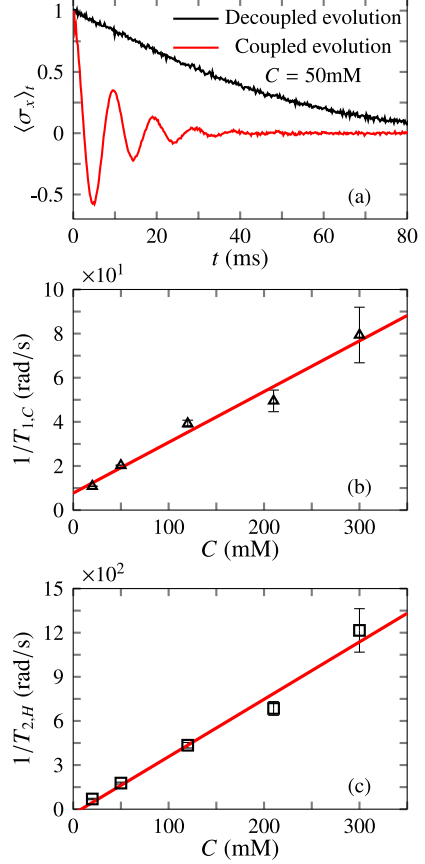


FIG. 1. (Color online) (a) Coupled and decoupled ^{13}C FID's for the 50mM concentration, showing the speedup of the decoherence due to scalar relaxation. The deviation from an exponential decay is the result of a small frequency offset. The dependence of $T_{1,H}$ (b) and $T_{2,C}$ (c) on the $\text{Fe}(\text{acac})_3$ concentration, exhibiting the well known linear dependence of the relaxation rate on the concentration of a paramagnetic species [47].

concentrations in which the system undergoes Markovian dynamics, we find that the WY metric sets the tighter QSL bound. However, for low concentrations, we observe non-Markovian dynamics, and the relative difference $\delta_\gamma^{\text{QFI}} - \delta_\gamma^{\text{WY}}$ [see Eq. (8)] exhibits crossovers between the geometric QSL bounds related to the QFI and WY metrics.

Results and discussion — In Fig. 1(a), we show the long decay of the ^{13}C FID when we decouple the ^{13}C and ^1H nuclear spins, which makes clear the effect of the ^1H as the main source of decoherence. This effect happens due to the longitudinal relaxation of the ^1H nuclear spin and the scalar J coupling having the same time scale. When $T_{1,H} \approx 1/J$, the random spin flips on the proton spin caused by the $T_{1,H}$ process make the scalar interaction effectively time-dependent, turning the ^1H into a source of decoherence for the ^{13}C . Thus, by changing the concentration of $\text{Fe}(\text{acac})_3$, we control the correlation time of the system-environment interaction.

In the presence of paramagnetic ions, the magnetic dipolar interaction of the nuclear spins with the spins of the ion's unpaired electrons is usually much stronger than with other nuclear spins. Thus paramagnetic relaxation becomes the pri-

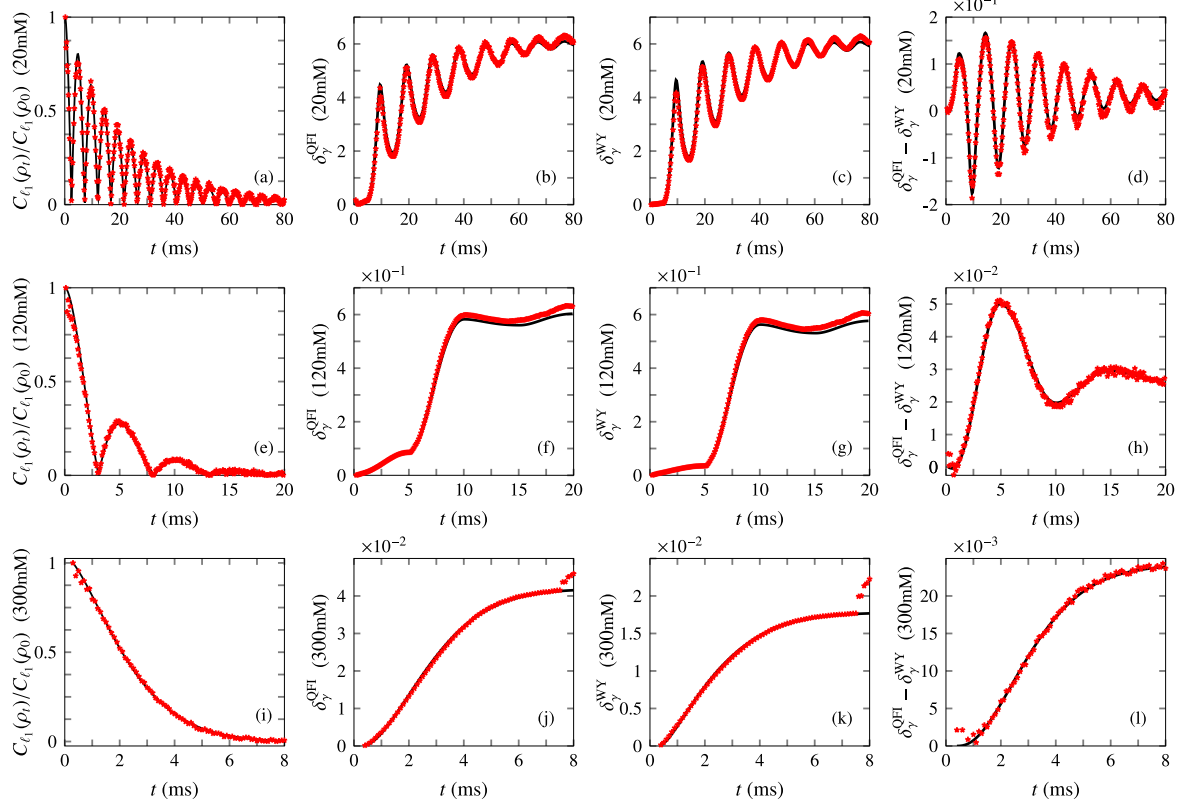


FIG. 2. (Color online) Plot of the normalized coherence measure $C_{\ell_1}(\rho_t)/C_{\ell_1}(\rho_0)$ (a,e,i); relative errors $\delta_{\gamma}^{\text{QFI}, \text{WY}}$ (b,c,f,g,j,k); and relative difference $\delta_{\gamma}^{\text{QFI}} - \delta_{\gamma}^{\text{WY}}$ (d,h,l), for the concentrations 20mM, 120mM and 300mM. The system is initialized at the single-qubit state $\rho_0 = (1/2)(\mathbb{I} + \langle \sigma_x \rangle_0 \sigma_x + \langle \sigma_z \rangle_0 \sigma_z)$, with $\langle \sigma_x \rangle_0 = \langle \sigma_z \rangle_0 = 1/\sqrt{2}$. Here, the experimental data is shown as red dots (●), while solid black lines (—) presented in each panel are the results obtained from the numerical simulations, setting the coupling strength $J = 209.1$ Hz, with $T_{1,H} = 7.1$ ms and $T_{2,C} = 38.55$ ms (a,b,c,d); $T_{1,H} = 1.15$ ms and $T_{2,C} = 12.8$ ms (e,f,g,h); $T_{1,H} = 0.425$ ms and $T_{2,C} = 5.49$ ms (i,j,k,l).

mary nuclear relaxation mechanism, scaling up the inverse of the average distance between the ions and the nucleus, resing in a linear dependence of the relaxation rates, $1/T_{1,H}$ and $1/T_{2,C}$, with the concentration of paramagnetic ions [47]. Figures 1(b) and 1(c) show the linear behavior for $1/T_{1,H}$ and $1/T_{2,C}$, as expected for paramagnetic relaxation.

We investigate the dynamical behavior of quantum coherence of the two-level system, thus characterizing non-Markovian and Markovian regimes based on the so-called ℓ_1 -norm of coherence [54]. Figures 2(a), 2(e), and 2(i) show the normalized ℓ_1 -norm of coherence of the evolved single-qubit state for different concentrations of $\text{Fe}(\text{acac})_3$, with $C_{\ell_1}(\rho_t) = \sum_{j \neq 1} |\langle j | \rho_t | j \rangle|$ [55, 56]. Here, we set $\{|0\rangle, |1\rangle\}$ as the reference basis to evaluate the coherence measure, with $\sigma_z |s\rangle = (-1)^s |s\rangle \forall s \in \{0, 1\}$. In Fig. 2(a), with $C = 20\text{mM}$, the normalized quantum coherence measure exhibits periodic revivals with damped amplitudes, thus vanishing at later times of the dynamics. Figure 2(e) shows a qualitatively similar behavior, with the quantum coherence approaching zero faster for $C = 120\text{mM}$. In both cases, the revivals point to the signature of non-Markovian dynamics. In Fig. 2(i), the quantum coherence displays a monotonic decay for $C = 300\text{mM}$, a typical behavior of Markovian dynamics [57]. Overall, from

low to high concentrations of the paramagnetic salt, we observe the non-Markovian regime for $T_{1,H} \approx 1/J$ (20mM and 120mM), while for $T_{1,H} \ll 1/J$ the dynamics is Markovian (300mM). The solid line depicts the best fit using the model given in Eq. (1). The measured values are $T_{1,H} = 12 \pm 1$ ms and $T_{2,C} = 480 \pm 20$ ms for $C = 20\text{mM}$; $T_{1,H} = 1.7 \pm 0.2$ ms and $T_{2,C} = 87 \pm 3$ ms for $C = 120\text{mM}$; and $T_{1,H} = 0.63 \pm 0.08$ ms and $T_{2,C} = 29 \pm 2$ ms for $C = 300\text{mM}$. In the numerical simulations, we used the coupling strength $J = 209.1$ Hz, with $T_{1,H} = 7.1$ ms and $T_{2,C} = 38.55$ ms for $C = 20\text{mM}$ [see Figs. 2(a)–2(d)]; $T_{1,H} = 1.15$ ms and $T_{2,C} = 12.8$ ms for $C = 120\text{mM}$ [see Figs. 2(e)–2(h)]; and $T_{1,H} = 0.425$ ms and $T_{2,C} = 5.49$ ms for $C = 300\text{mM}$ [see Figs. 2(i)–2(l)]. The large discrepancy between the measured and simulated values is mainly due to frequency offset errors, which accelerate the signal decay and lead to shorter $T_{1,H}$ and $T_{2,C}$ for fitted values. Such errors come from difficulty in setting the exact resonance frequency when the spectral lines are broad due to the fast relaxation rates used in the experiments. The system initiates at the state $\rho_0 = (1/2)(\mathbb{I} + (\sigma_x + \sigma_z)/\sqrt{2})$.

Fig. 2 shows the relative error δ_{γ}^f [see Eq. (8)] for the speed limit time for both QFI [Figs. 2(b), 2(f), and 2(j)] and WY [Figs. 2(c), 2(g), and 2(k)] metrics. These quantities are very

sensitive to noise since even the small fluctuations observed for short times in the signals of 120 and 300 mM concentrations heavily affect δ_γ^f . This happens due to the time-derivative in Eq. (3). Thus, to avoid undesired numerical errors, we smoothed the data before the numerical integration to evaluate ℓ_γ^f for both metrics. The results are shown in the Supplementary Material without smoothing the data. Figures 2(b) and 2(c) show the relative errors $\delta_\gamma^{\text{QFI}}$ and $\delta_\gamma^{\text{WY}}$ within the non-Markovian regime of the dynamics, with $C = 20\text{mM}$. These relative errors oscillate out of phase with the FID signal. Next, for $C = 120\text{mM}$, Figs. 2(f) and 2(g) show each relative error with a non-monotonic behavior, a fingerprint of non-Markovianity for non-unitary evolution. Figures 2(j) and 2(k) show that for $C = 300\text{mM}$, both relative errors behave monotonically as a function of the evolution time of the Markovian dynamics.

To investigate the tightness of the quantum speed limit, we plot in Figs. 2(d), 2(h), and 2(l) the relative difference $\delta_\gamma^{\text{QFI}} - \delta_\gamma^{\text{WY}}$ for the concentrations 20mM, 120mM and 300mM, respectively. Importantly, for $\delta_\gamma^{\text{QFI}} - \delta_\gamma^{\text{WY}} > 0$, one finds the tighter speed limit signaled by the WY metric. Otherwise, for $\delta_\gamma^{\text{QFI}} - \delta_\gamma^{\text{WY}} < 0$, the QFI metric systematically produces the tightest lower bound to the evolution time. For $C = 20\text{mM}$, Fig. 2(d) shows that the relative difference oscillates over the evolution time and exhibits crossovers between $\delta_\gamma^{\text{QFI}}$ and $\delta_\gamma^{\text{WY}}$, and both QFI and WY metrics give rise to the same geometric QSL whenever $\delta_\gamma^{\text{QFI}} - \delta_\gamma^{\text{WY}} = 0$. No crossover occurs after $t \sim 57.4\text{ ms}$, and the QSL related to the WY metric turns out to be the tighter one at later times of the dynamics. The tightest geometric QSL is captured by the Wigner-Yanase skew information metric for the two higher concentrations, even for the non-Markovian regime observed for the 120 mM concentration. This is seen in Figs. 2(h) and 2(l).

Conclusions — In summary, we experimentally assess ge-

ometric speed limits for the nonunitary dynamics of a qubit encoded on ^{13}C nuclear spin. We control the relaxation rates of the qubit by adding $\text{Fe}(\text{acac})_3$ to the solution. The paramagnetic relaxation makes it possible to vary the relaxation times by two orders of magnitude, and we could observe a transition between non-Markovian to Markovian regimes in the nonunitary reduced dynamics of ^{13}C spins depending on the salt concentrations. Taking a geometric approach to address the QSL based on the quantum Fisher information and Wigner-Yanase skew information metrics, we find a good agreement between the results of numerical simulations and the experiment. For high concentrations, we found that the WY metric sets the tighter QSL instead of the QFI for Markovian or non-Markovian dynamics. For low concentrations (20mM), we observe nontrivial crossovers between the geometric QSLs defined by the QFI and WY metrics, while the system exhibits non-Markovian dynamics. In this setting, a different metric (QFI or WY) sets the tighter QSL during a time window closely related to the zeros of the spin magnetization along the x -axis. Furthermore, at later times, the WY metric signals the tighter QSL as the crossovers no longer occur. We remark how geometric QSLs are very sensitive to noise, i.e., even tiny fluctuations observed for short times in the data, from low to high concentrations, heavily affect the figure of merit that signals the speed of evolution of the two-level system.

Acknowledgments — This work was supported by the Brazilian ministries MEC and MCTIC, and the Brazilian funding agencies CNPq (Grant No. 304891/2022-3), FAPESP (Grant No. 2017/03727-0), Coordenação de Aperfeiçoamento de Pessoal de Nível Superior–Brasil (CAPES) (Finance Code 001), and the Brazilian National Institute of Science and Technology of Quantum Information (INCT-IQ). D. P. P. also acknowledges Fundação de Amparo à Pesquisa e ao Desenvolvimento Científico e Tecnológico do Maranhão (FAPEMA).

[1] Y. Aharonov and D. Bohm, “Time in the Quantum Theory and the Uncertainty Relation for Time and Energy,” *Phys. Rev.* **122**, 1649 (1961).

[2] P. Pfeifer and J. Fröhlich, “Generalized time-energy uncertainty relations and bounds on lifetimes of resonances,” *Rev. Mod. Phys.* **67**, 759 (1995).

[3] L. Mandelstam and I. Tamm, “The uncertainty relation between energy and time in non-relativistic quantum mechanics,” in *Selected Papers*, edited by B. M. Bolotovskii, V. Y. Frenkel, and R. Peierls (Springer, Berlin, Heidelberg, 1991) pp. 115–123.

[4] N. Margolus and L. B. Levitin, “The maximum speed of dynamical evolution,” *Physica D* **120**, 188 (1998).

[5] F. Campaioli, F. A. Pollock, and K. Modi, “Tight, robust, and feasible quantum speed limits for open dynamics,” *Quantum* **3**, 168 (2019).

[6] F. Campaioli, C.-S. Yu, F. A. Pollock, and K. Modi, “Resource speed limits: Maximal rate of resource variation,” *New J. Phys.* **24**, 065001 (2022).

[7] E. O’Connor, G. Guarnieri, and S. Campbell, “Action quantum speed limits,” *Phys. Rev. A* **103**, 022210 (2021).

[8] B. Mohan, S. Das, and A. K. Pati, “Quantum speed limits for information and coherence,” *New J. Phys.* **24**, 065003 (2022).

[9] D. P. Pires, “Unified entropies and quantum speed limits for nonunitary dynamics,” *Phys. Rev. A* **106**, 012403 (2022).

[10] M. M. Taddei, B. M. Escher, L. Davidovich, and R. L. de Matos Filho, “Quantum speed limit for physical processes,” *Phys. Rev. Lett.* **110**, 050402 (2013).

[11] A. del Campo, I. L. Egusquiza, M. B. Plenio, and S. F. Huelga, “Quantum speed limits in open system dynamics,” *Phys. Rev. Lett.* **110**, 050403 (2013).

[12] M. Okuyama and M. Ohzeki, “Quantum Speed Limit is Not Quantum,” *Phys. Rev. Lett.* **120**, 070402 (2018).

[13] R. Hamazaki, “Speed Limits for Macroscopic Transitions,” *PRX Quantum* **3**, 020319 (2022).

[14] F. Impens, F. M. D’Angelis, F. A. Pinheiro, and D. Guéry-Odelin, “Time scaling and quantum speed limit in non-Hermitian Hamiltonians,” *Phys. Rev. A* **104**, 052620 (2021).

[15] L. Lokutsievskiy and A. Pechen, “Reachable sets for two-level open quantum systems driven by coherent and incoherent controls,” *J. Phys. A: Math. Theor.* **54**, 395304 (2021).

[16] G. Ness, A. Alberti, and Y. Sagi, “Quantum Speed Limit for States with a Bounded Energy Spectrum,” *Phys. Rev. Lett.* **129**,

140403 (2022).

[17] Y. Shao, B. Liu, M. Zhang, H. Yuan, and J. Liu, “Operational definition of a quantum speed limit,” *Phys. Rev. Research* **2**, 023299 (2020).

[18] K. Kobayashi and N. Yamamoto, “Quantum speed limit for robust state characterization and engineering,” *Phys. Rev. A* **102**, 042606 (2020).

[19] R. Puebla, S. Deffner, and S. Campbell, “Kibble-Zurek scaling in quantum speed limits for shortcuts to adiabaticity,” *Phys. Rev. Research* **2**, 032020 (2020).

[20] B. Mohan and A. K. Pati, “Reverse quantum speed limit: How slowly a quantum battery can discharge,” *Phys. Rev. A* **104**, 042209 (2021).

[21] T. Fogarty, S. Deffner, T. Busch, and S. Campbell, “Orthogonality Catastrophe as a Consequence of the Quantum Speed Limit,” *Phys. Rev. Lett.* **124**, 110601 (2020).

[22] A. del Campo, “Probing Quantum Speed Limits with Ultracold Gases,” *Phys. Rev. Lett.* **126**, 180603 (2021).

[23] M. R. Lam, N. Peter, T. Groh, W. Alt, C. Robens, D. Meschede, A. Negretti, S. Montangero, T. Calarco, and A. Alberti, “Demonstration of Quantum Brachistochrones between Distant States of an Atom,” *Phys. Rev. X* **11**, 011035 (2021).

[24] L. P. García-Pintos, S. B. Nicholson, J. R. Green, A. del Campo, and A. V. Gorshkov, “Unifying Quantum and Classical Speed Limits on Observables,” *Phys. Rev. X* **12**, 011038 (2022).

[25] D. P. Pires, K. Modi, and L. C. Céleri, “Bounding generalized relative entropies: Nonasymptotic quantum speed limits,” *Phys. Rev. E* **103**, 032105 (2021).

[26] Y. Hasegawa, “Unifying speed limit, thermodynamic uncertainty relation and Heisenberg principle via bulk-boundary correspondence,” *Nat. Commun.* **14**, 2828 (2023).

[27] E. Aghion and J. R. Green, “Thermodynamic speed limits for mechanical work,” *J. Phys. A: Math. Theor.* **56**, 05LT01 (2023).

[28] D. P. Pires and T. R. de Oliveira, “Relative purity, speed of fluctuations, and bounds on equilibration times,” *Phys. Rev. A* **104**, 052223 (2021).

[29] D. P. Pires, M. Cianciaruso, L. C. Céleri, G. Adesso, and D. O. Soares-Pinto, “Generalized Geometric Quantum Speed Limits,” *Phys. Rev. X* **6**, 021031 (2016).

[30] S. Deffner and S. Campbell, “Quantum speed limits: from Heisenberg’s uncertainty principle to optimal quantum control,” *J. Phys. A: Math. Theor.* **50**, 453001 (2017).

[31] K. Lan, S. Xie, and X. Cai, “Geometric quantum speed limits for Markovian dynamics in open quantum systems,” *New J. Phys.* **24**, 055003 (2022).

[32] S. Deffner and E. Lutz, “Quantum Speed Limit for Non-Markovian Dynamics,” *Phys. Rev. Lett.* **111**, 010402 (2013).

[33] Z.-Y. Xu and S.-Q. Zhu, “Quantum Speed Limit of a Photon under Non-Markovian Dynamics,” *Chinese Phys. Lett.* **31**, 020301 (2014).

[34] Z. Sun, J. Liu, J. Ma, and X. Wang, “Quantum speed limits in open systems: Non-Markovian dynamics without rotating-wave approximation,” *Sci. Rep.* **5**, 8444 (2015).

[35] X. Meng, C. Wu, and H. Guo, “Minimal evolution time and quantum speed limit of non-Markovian open systems,” *Sci. Rep.* **5**, 16357 (2015).

[36] N. Mirkin, F. Toscano, and D. A. Wisniacki, “Quantum-speed-limit bounds in an open quantum evolution,” *Phys. Rev. A* **94**, 052125 (2016).

[37] Y.-J. Zhang, Y.-J. Xia, and H. Fan, “Control of quantum dynamics: Non-Markovianity and the speedup of the open system evolution,” *EPL (Europhysics Letters)* **116**, 30001 (2016).

[38] A. Rivas, S. F. Huelga, and M. B. Plenio, “Quantum non-Markovianity: characterization, quantification and detection,” *Rep. Prog. Phys.* **77**, 094001 (2014).

[39] Z.-Y. Xu, S. Luo, W. L. Yang, C. Liu, and S. Zhu, “Quantum speedup in a memory environment,” *Phys. Rev. A* **89**, 012307 (2014).

[40] M. Cianciaruso, S. Maniscalco, and G. Adesso, “Role of non-Markovianity and backflow of information in the speed of quantum evolution,” *Phys. Rev. A* **96**, 012105 (2017).

[41] J. Teittinen, H. Lyyra, and S. Maniscalco, “There is no general connection between the quantum speed limit and non-Markovianity,” *New J. Phys.* **21**, 123041 (2019).

[42] G. Ness, M. R. Lam, W. Alt, D. Meschede, Y. Sagi, and A. Alberti, “Observing crossover between quantum speed limits,” *Sci. Adv.* **7**, 9119 (2021).

[43] D. V. Villamizar, E. I. Duzzioni, A. C. S. Leal, and R. Auccaise, “Estimating the time evolution of NMR systems via a quantum-speed-limit-like expression,” *Phys. Rev. A* **97**, 052125 (2018).

[44] Y. Kondo, Y. Matsuzaki, K. Matsushima, and J. G. Filgueiras, “Using the quantum Zeno effect for suppression of decoherence,” *New J. Phys.* **18**, 013033 (2016).

[45] L. B. Ho, Y. Matsuzaki, M. Matsuzaki, and Y. Kondo, “Nuclear Magnetic Resonance Model of an Entangled Sensor under Noise,” *J. Phys. Soc. Japan* **89**, 054001 (2020).

[46] A. Iwakura, Y. Matsuzaki, and Y. Kondo, “Engineered noisy environment for studying decoherence,” *Phys. Rev. A* **96**, 032303 (2017).

[47] A. Abragam, *The Principles of Nuclear Magnetism*, International series of monographs on physics (Clarendon Press, 1961).

[48] L. B. Ho, Y. Matsuzaki, M. Matsuzaki, and Y. Kondo, “Realization of controllable open system with NMR,” *New J. Phys.* **21**, 093008 (2019).

[49] Supplemental Material at [URL will be inserted by publisher] for technical details about the experiment and sample preparation, and details on the derivation of geometric QSLs.

[50] Z. Zhou, R. Kummerle, X. Qiu, D. Redwine, R. Cong, A. Taha, D. Baugh, and B. Winniford, “A new decoupling method for accurate quantification of polyethylene copolymer composition and triad sequence distribution with ^{13}C NMR,” *J. Magn. Reson.* **187**, 225 (2007).

[51] E. A. Morozova and N. N. Čencov, “Markov Invariant Geometry on Manifolds of States,” *J. Sov. Math.* **56**, 2648 (1991).

[52] D. Petz, “Monotone metrics on matrix spaces,” *Linear Algebra Appl.* **244**, 81 (1996).

[53] J. Anandan and Y. Aharonov, “Geometry of quantum evolution,” *Phys. Rev. Lett.* **65**, 1697 (1990).

[54] K.-D. Du, Z. Hou, G.-Y. Xiang, C.-F. Li, G.-C. Guo, D. Dong, and F. Nori, “Detecting non-Markovianity via quantified coherence: theory and experiments,” *npj Quantum Inf.* **6**, 55 (2020).

[55] T. Baumgratz, M. Cramer, and M. B. Plenio, “Quantifying Coherence,” *Phys. Rev. Lett.* **113**, 140401 (2014).

[56] A. Streltsov, G. Adesso, and M. B. Plenio, “Colloquium: Quantum coherence as a resource,” *Rev. Mod. Phys.* **89**, 041003 (2017).

[57] H. P. Breuer, E. M. Laine, and J. Piilo, “Measure for the degree of non-markovian behavior of quantum processes in open systems,” *Phys. Rev. Lett.* **103**, 210401 (2009).

[58] M. Nielsen and I. L. Chuang, *Quantum Computation and Quantum Information: 10th Anniversary Edition* (Cambridge University Press, Cambridge, 2010).

[59] I. Bengtsson and K. Życzkowski, *Geometry of Quantum States: An Introduction to Quantum Entanglement* (Cambridge University Press, Cambridge, 2006)

Supplementary Material

I. QSL FOR GENERAL SINGLE-QUBIT STATES

In the following, we provide analytical expressions for the length $\ell_\gamma^f(\rho_0, \rho_\tau)$ of the path γ drawn by the evolution of the time-dependent single-qubit state $\rho_t = (1/2)(\mathbb{I} + \sum_{l=x,y,z} \langle \sigma_l \rangle_t \sigma_l)$, where σ_l is the l th Pauli matrix, while $\langle \sigma_l \rangle_t = \text{Tr}(\rho_t \sigma_l)$ defines the time-dependent magnetization along the l -axis, and \mathbb{I} is the identity matrix. The spectral decomposition of such state is given by $\rho_t = \sum_{s=\pm} p_s |\Psi_s\rangle\langle\Psi_s|$, with the eigenvalues

$$p_\pm = \frac{1}{2} \left(1 \pm \sqrt{\sum_{l=x,y,z} \langle \sigma_l \rangle_t^2} \right), \quad (\text{S1})$$

and the respective set of eigenstates

$$|\Psi_\pm\rangle = \frac{\left(\langle \sigma_z \rangle_t \pm \sqrt{\sum_{l=x,y,z} \langle \sigma_l \rangle_t^2} \right) |0\rangle + (\langle \sigma_x \rangle_t + i\langle \sigma_y \rangle_t) |1\rangle}{\sqrt{2 \left(\sum_{l=x,y,z} \langle \sigma_l \rangle_t^2 \pm \langle \sigma_z \rangle_t \sqrt{\sum_{l=x,y,z} \langle \sigma_l \rangle_t^2} \right)}}, \quad (\text{S2})$$

with $\{|0\rangle, |1\rangle\}$ being the eigenstates of the Pauli matrix σ_z , i.e., $\sigma_z |s\rangle = (-1)^s |s\rangle$, for all $s \in \{0, 1\}$. In addition, note that $\langle \Psi_k | \Psi_l \rangle = \delta_{k,l}$, and $\sum_{l=\pm} |\Psi_l\rangle\langle\Psi_l| = \mathbb{I}$. We emphasize that eigenvalues $p_s \equiv p_s(t)$ and eigenvectors $|\Psi_s\rangle \equiv |\Psi_s(t)\rangle$ of the density matrix are time-dependent quantities. In this setting, according to the Morozova-Čencov theorem, the length of the path depicted by ρ_t that connects initial ρ_0 and final ρ_τ states is written as follows [29, 52]

$$\ell_\gamma^f(\rho_0, \rho_\tau) = \int_0^\tau dt \sqrt{\mathcal{F}_t + Q_t^f}, \quad (\text{S3})$$

with

$$\begin{aligned} \mathcal{F}_t &= \frac{1}{4} \sum_{k=\pm} \frac{1}{p_k} \left(\frac{dp_k}{dt} \right)^2 \\ &= \frac{\left(\sum_{l=x,y} \langle \sigma_l \rangle_t (d\langle \sigma_l \rangle_t / dt) \right)^2}{4 \left(\sum_{l=x,y,z} \langle \sigma_l \rangle_t^2 \right) \left(1 - \sum_{l=x,y,z} \langle \sigma_l \rangle_t^2 \right)}, \end{aligned} \quad (\text{S4})$$

and also

$$\begin{aligned} Q_t^f &= -\frac{1}{2} c_f(p_+, p_-) (p_+ - p_-)^2 \langle \Psi_+ | \frac{d}{dt} | \Psi_- \rangle \langle \Psi_- | \frac{d}{dt} | \Psi_+ \rangle \\ &= \frac{c_f(p_+, p_-) \left[\left(\sum_{j,l=x,y} (\delta_{j,x} \delta_{l,y} - \delta_{j,y} \delta_{l,x}) \langle \sigma_j \rangle_t (d\langle \sigma_l \rangle_t / dt) \right)^2 + \langle \sigma_z \rangle_t^2 \left(\sum_{l=x,y} (d\langle \sigma_l \rangle_t / dt)^2 \right) \right]}{8 \left(\sum_{l=x,y,z} \langle \sigma_l \rangle_t^2 \right)}, \end{aligned} \quad (\text{S5})$$

where $c_f(x, y) = 1/[yf(x/y)]$ is a symmetric function, while f stands for the Morozova-Čencov (MC) function. We remind that a chosen MC function $f : (0, \infty) \rightarrow (0, \infty)$ is (i) operator monotone, i.e., for semi-positive definite operators satisfying $B - A \geq 0$, it follows that $f(B) \geq f(A)$; (ii) self-inversive, $f(x/y) = (x/y)f(y/x)$; (iii) normalized, i.e., $f(1) = 1$ [51]. We note that the quantity \mathcal{F}_t in Eq. (S4) is related to the so-called Fisher-Rao metric, and depends on the populations of the single-qubit state. In turn, the function Q_t^f in Eq. (S5) is related to the coherences of the density matrix, and its evaluation depends on the choice of a given MC function that sets a Riemannian metric over the space of quantum states.

In the following, we specialize Eq. (S5) by setting the quantum Fisher information (QFI) metric, with $f_{\text{QFI}}(u) = (u + 1)/2$, and also the Wigner-Yanase skew information (WY) metric, with $f_{\text{WY}}(u) = (\sqrt{u} + 1)^2/4$. For the QFI metric, given that $c_{\text{QFI}}(p_+, p_-) = 2/(p_+ + p_-) = 2$ [see Eq. (S1)], we find that

$$Q_t^{\text{QFI}} = \frac{\left(\sum_{j,l=x,y} (\delta_{j,x} \delta_{l,y} - \delta_{j,y} \delta_{l,x}) \langle \sigma_j \rangle_t (d\langle \sigma_l \rangle_t / dt) \right)^2 + \langle \sigma_z \rangle_t^2 \left(\sum_{l=x,y} (d\langle \sigma_l \rangle_t / dt)^2 \right)}{4 \left(\sum_{l=x,y,z} \langle \sigma_l \rangle_t^2 \right)}. \quad (\text{S6})$$

In addition, for the WY metric with $c_{\text{WY}}(p_+, p_-) = 4/(\sqrt{p_+} + \sqrt{p_-})^2$ [see Eq. (S1)], we obtain the result

$$Q_t^{\text{WY}} = \frac{\left(\sum_{j,l=x,y} (\delta_{j,x}\delta_{l,y} - \delta_{j,y}\delta_{l,x}) \langle\sigma_j\rangle_t (d\langle\sigma_l\rangle_t/dt)\right)^2 + \langle\sigma_z\rangle_t^2 \left(\sum_{l=x,y} (d\langle\sigma_l\rangle_t/dt)^2\right)}{2 \left(\sum_{l=x,y,z} \langle\sigma_l\rangle_t^2\right) \left(1 + \sqrt{1 - \sum_{l=x,y,z} \langle\sigma_l\rangle_t^2}\right)}. \quad (\text{S7})$$

It is known that the length $\ell_\gamma^f(\rho_0, \rho_\tau)$ of the path γ connecting the initial and final states need not to be the shortest one [29, 53]. Indeed, the MCP theorem assigns a certain geodesic length $\mathcal{L}_\gamma^f(\rho_0, \rho_\tau)$ to each contractive metric that equips the space of quantum states, with $\mathcal{L}_\gamma^f(\rho_0, \rho_\tau) \leq \ell_\gamma^f(\rho_0, \rho_\tau)$. In this setting, for the QFI metric, its geodesic length is given by the so-called Bures angle, i.e., $\mathcal{L}^{\text{QFI}}(\rho_0, \rho_\tau) = \arccos[\sqrt{F(\rho_0, \rho_\tau)}]$, where $F(\rho_0, \rho_\tau) = \|\sqrt{\rho_0} \sqrt{\rho_\tau}\|_1^2$ is the Uhlmann fidelity, and $\|A\|_1 = \text{Tr}(\sqrt{A^\dagger A})$ sets the Schatten 1-norm [58]. It can be cast as follows

$$\mathcal{L}^{\text{QFI}}(\rho_0, \rho_\tau) = \arccos\left(\frac{\sqrt{2}}{2} \sqrt{1 + \sum_{l=x,y,z} \langle\sigma_l\rangle_0 \langle\sigma_l\rangle_\tau + \prod_{s=0,\tau} \sqrt{1 - \sum_{l=x,y,z} \langle\sigma_l\rangle_s^2}}\right). \quad (\text{S8})$$

In turn, the so-called Hellinger angle $\mathcal{L}^{\text{WY}}(\rho_0, \rho_\tau) = \arccos[A(\rho_0, \rho_\tau)]$ stands for the geodesic length related to the Wigner-Yanase skew information metric, where $A(\rho_0, \rho_\tau) = \text{Tr}(\sqrt{\rho_0} \sqrt{\rho_\tau})$ defines the quantum affinity [59]. In particular, it becomes

$$\mathcal{L}^{\text{WY}}(\rho_0, \rho_\tau) = \arccos\left\{\frac{\sum_{l=x,y,z} \langle\sigma_l\rangle_0 \langle\sigma_l\rangle_\tau + \prod_{s=0,\tau} \left(1 + \sqrt{1 - \sum_{l=x,y,z} \langle\sigma_l\rangle_s^2}\right)}{\prod_{s=0,\tau} \left(\sqrt{1 + \sqrt{\sum_{l=x,y,z} \langle\sigma_l\rangle_s^2}} + \sqrt{1 - \sqrt{\sum_{l=x,y,z} \langle\sigma_l\rangle_s^2}}\right)}\right\}. \quad (\text{S9})$$

Next, we specialize the results in Eqs. (S3), (S4), (S6), (S7), (S8) and (S9) to the case of a single-qubit state with $\langle\sigma_x\rangle_t \neq 0$, $\langle\sigma_y\rangle_t = 0$, and $\langle\sigma_z\rangle_t = \langle\sigma_z\rangle_0$, for all $t \geq 0$. We shall be with the lengths $\ell_\gamma^{\text{QFI}}(\rho_0, \rho_\tau)$ and $\ell_\gamma^{\text{WY}}(\rho_0, \rho_\tau)$ related to both QFI and WY metrics, respectively, which can be written as

$$\ell_\gamma^f(\rho_0, \rho_\tau) = \frac{1}{2} \int_0^\tau dt \sqrt{h_t^f} \left| \frac{d\langle\sigma_x\rangle_t}{dt} \right|, \quad (\text{S10})$$

with

$$h_t^{\text{QFI}} := \frac{1 - \langle\sigma_z\rangle_0^2}{1 - \langle\sigma_x\rangle_t^2 - \langle\sigma_z\rangle_0^2}, \quad (\text{S11})$$

and

$$h_t^{\text{WY}} = \frac{\langle\sigma_x\rangle_t^2}{\langle\sigma_x\rangle_t^2 + \langle\sigma_z\rangle_0^2} \left(1 - \langle\sigma_x\rangle_t^2 - \langle\sigma_z\rangle_0^2\right) + \frac{2\langle\sigma_z\rangle_0^2 \left(1 - \sqrt{1 - \langle\sigma_x\rangle_t^2 - \langle\sigma_z\rangle_0^2}\right)}{\left(\langle\sigma_x\rangle_t^2 + \langle\sigma_z\rangle_0^2\right)^2}. \quad (\text{S12})$$

We now address the geodesic lengths related to QFI and WY metrics in Eqs. (S8) and (S9), respectively. In turn, the Bures angle becomes

$$\mathcal{L}^{\text{QFI}}(\rho_0, \rho_\tau) = \arccos\left(\frac{\sqrt{2}}{2} \sqrt{1 + \langle\sigma_x\rangle_0 \langle\sigma_x\rangle_\tau + \langle\sigma_z\rangle_0^2 + \sqrt{(1 - \langle\sigma_x\rangle_0^2 - \langle\sigma_z\rangle_0^2)(1 - \langle\sigma_x\rangle_\tau^2 - \langle\sigma_z\rangle_0^2)}}\right), \quad (\text{S13})$$

while the Hellinger angle yields

$$\begin{aligned} \mathcal{L}^{\text{WY}}(\rho_0, \rho_\tau) = & \\ \arccos\left\{\frac{\langle\sigma_x\rangle_0 \langle\sigma_x\rangle_\tau + \langle\sigma_z\rangle_0^2 + \left(1 + \sqrt{1 - \langle\sigma_x\rangle_0^2 - \langle\sigma_z\rangle_0^2}\right) \left(1 + \sqrt{1 - \langle\sigma_x\rangle_\tau^2 - \langle\sigma_z\rangle_0^2}\right)}{\left(\sqrt{1 + \sqrt{\langle\sigma_x\rangle_0^2 + \langle\sigma_z\rangle_0^2}} + \sqrt{1 - \sqrt{\langle\sigma_x\rangle_0^2 + \langle\sigma_z\rangle_0^2}}\right) \left(\sqrt{1 + \sqrt{\langle\sigma_x\rangle_\tau^2 + \langle\sigma_z\rangle_0^2}} + \sqrt{1 - \sqrt{\langle\sigma_x\rangle_\tau^2 + \langle\sigma_z\rangle_0^2}}\right)}\right\}. \end{aligned} \quad (\text{S14})$$

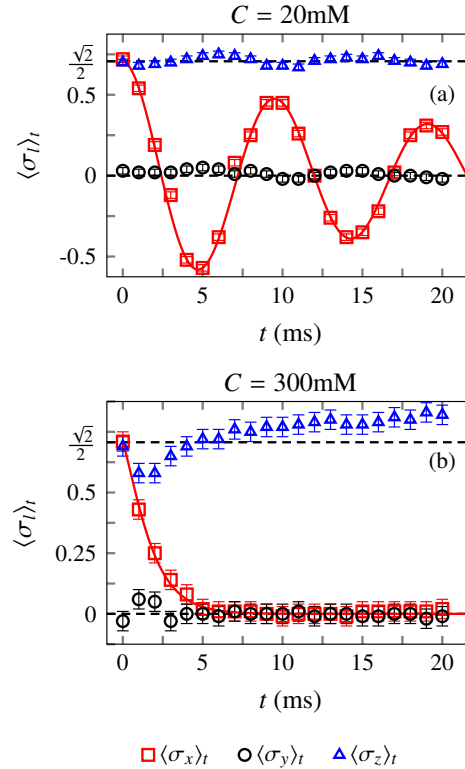


FIG. S1. (Color online) Plot of the quantum state tomographies for the concentrations of 20mM (upper panel) and 300mM (lower panel) for the evolved state ρ_t^C of the two-level system. The red solid lines depict the numerical simulation of theoretical predictions for each magnetization $\langle \sigma_l \rangle_t = \text{Tr}(\sigma_l \rho_t^C)$, for all $l = \{x, y, z\}$, with (a) $T_{1,H} = (7.2 \pm 0.3)$ ms and $T_{2,C} = (46 \pm 6)$ ms; (b) $T_{1,H} = (0.730 \pm 0.003)$ ms and $T_{2,C} = (6.3 \pm 0.2)$ ms.

II. METHODS

Here, we discuss technical details of the experiment. We carried out the measurements at 25° C in a Bruker Avance III 600 MHz, with ^1H and ^{13}C Larmor frequencies of 600 and 150 MHz, respectively, with a 5 mm double resonance probe-head. We realized the experiments with a solution of chloroform (CHCl_3), with natural abundance of ^{13}C in a 5 mm NMR tube, doped with Iron(III) acetylacetone ($\text{Fe}(\text{acac})_3$, Sigma Aldrich). To guarantee good frequency stability, we used the deuterium signal of acetone-d6 (Cambridge Isotopes Laboratories - Inc.) to lock the NMR signal. We avoided the undesired line broadening of the deuterium reference signal, due to the effects of the paramagnetic salt, putting the acetone-d6 in a 3 mm NMR tube, all inside the 5 mm tube.

We prepared the solutions of CHCl_3 and Iron(III) acetylacetone diluting the paramagnetic salt in 2 ml of CHCl_3 . To get the concentrations of 20, 50, 120, 300 and 450 mM, we used 14.5(1), 35.5(1), 85.1(1), 211.6(1) and 317.8(1) miligrams of $\text{Fe}(\text{acac})_3$, respectively. The error on the concentrations is of 1 mM. Each sample contained 150 μl of doped CHCl_3 and 150 μl of acetone-d6.

We measured the spin-lattice relaxation rate $T_{1,H}$ for ^1H and ^{13}C using a standard inversion-recovery pulse sequence and the ^{13}C spin-spin relaxation rate $T_{2,C}$ from the Free Induction Decay (FID) signal obtained when both spins are decoupled through a Waltz-64 heteronuclear decoupling sequence [50], with a decoupling $\pi/2$ -pulse of 54 μs . We assumed $T_{2,C} \approx T_{2,C}^*$ due to a good shimming. To avoid frequency offset effects on the estimation of $T_{2,C}$, the FID signals were fitted using a function $M_x(t) = M_0 e^{-t/T_{2,C}} \cos(\omega t)$, where M_0 is the initial magnetization amplitude and ω is the frequency offset. We used the spectrum of the thermal equilibrium state to adjust the phase and normalize the intensity of all NMR data throughout this work.

Figure S1 shows the time evolution of the initial state during the decoherence process for two concentrations. In Fig. S1(a), with a low concentration of 20 mM of $\text{Fe}(\text{acac})_3$, we observe the revivals of the $\langle \sigma_x \rangle_t$ component due to the non-Markovian regime, indicating the information backflow from the environment to the system that is characteristic of strong non-Markovianity [57]. Note that $\langle \sigma_y \rangle_t \approx 0$ and $\langle \sigma_z \rangle_t \approx \sqrt{2}/2$ remains constant throughout the decoherence process, which means that any time-dependent quantity can be uniquely described by the evolution of $\langle \sigma_x \rangle_t$. In turn, Fig. S1(b) display the FID signal for concentration 300 mM. As such, we can use the FID data, i.e., $\langle \sigma_x \rangle_t$ to compute the geometric quantities of interest to

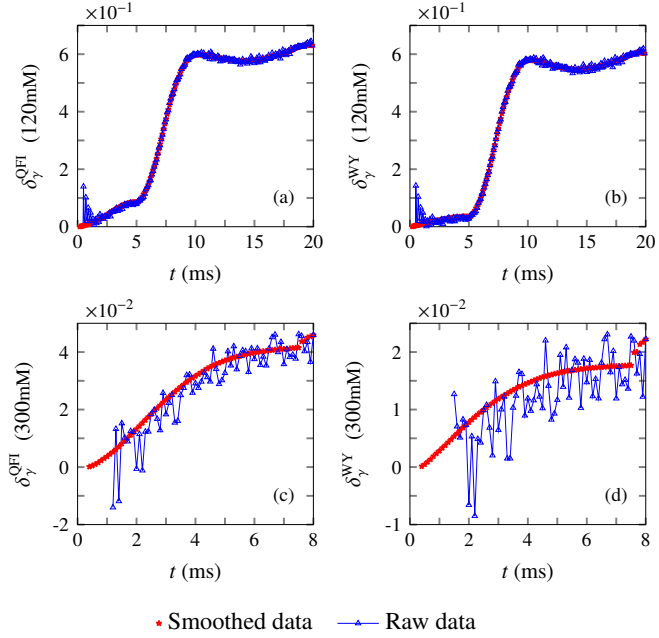


FIG. S2. (Color online) Plot of the relative errors $\delta_\gamma^{\text{QFI}}$ and $\delta_\gamma^{\text{WY}}$ [see Eq. (S15)] for the concentrations of 120mM (upper panels) and 300mM (lower panels). The blue triangular points correspond to the relative errors obtained from the original experimentally measured FID signal. The red dotted points depict the relative errors by using the smoothed FID data after noise subtraction.

evaluate the geometric QSL's, namely the length ℓ_γ^f , the geodesic distance \mathcal{L}^f , and the following relative difference

$$\delta_\gamma^f := \frac{\ell_\gamma^f(\rho_0, \rho_\tau) - \mathcal{L}^f(\rho_0, \rho_\tau)}{\mathcal{L}^f(\rho_0, \rho_\tau)} . \quad (\text{S15})$$

In Fig. S2, we show the relative errors $\delta_\gamma^{\text{QFI}}$ and $\delta_\gamma^{\text{WY}}$ for the concentration $C = 120\text{mM}$, with $T_{1,H} = 1.15$ ms and $T_{2,C} = 12.8$ ms [see Figs. S2(a) and S2(b)]; and $C = 300\text{mM}$, with $T_{1,H} = 0.425$ ms and $T_{2,C} = 5.49$ ms [see Figs. S2(c) and S2(d)]. Here we set the coupling strength $J = 209.1$ Hz. The blue triangular points depict the relative error obtained with the numerical simulation using the raw data of the original experimentally measured FID signal. The red dotted points depict the relative errors but using the smoothed FID data with noise subtraction. We emphasize that the relative error δ_γ^f in Eq. (S15) depends on the geodesic length \mathcal{L}^f and the length ℓ_γ^f for both QFI and WY metrics. In turn, Eq. (S10) shows that the evaluation of ℓ_γ^f requires numerical integration of the time-derivative of the FID signal, weighted by the square root of the auxiliary function h_t^f [see Eqs. (S11) and (S12)]. Overall, the time-derivative of the experimental data introduces undesired numerical errors that start to propagate over each step of the integration, causing a large deviation of ℓ_γ^f from its theoretical prediction. Indeed, as shown in Figs. S2(c) and S2(d), this effect is more pronounced for concentration 300mM. We improve the results by smoothing the FID, that is, subtracting the noise from the input data, before evaluating the aforementioned time-derivative and numerical integration.